SIMULATION OF SHOCK WAVES IN THE INTERPLANETARY MEDIUM

S. Poedts[1], B. Van der Holst[1], I. Chattopadhyay[1], D. Banerjee[1], T. Van Lier[1], and R. Keppens[2]

[1]CPA, K.U.Leuven, Celestijnenlaan 200B, 3001 Leuven, Belgium
[2]FOM Inst. for Plasma Physics Rijnhuizen, Nieuwegein, NL

ABSTRACT

The shocks in the solar corona and interplanetary (IP) space caused by fast Coronal Mass Ejections (CMEs) are simulated numerically and their structure and evolution is studied in the framework of magnetohydrodynamics (MHD). Due to the presence of three characteristic velocities and the anisotropy induced by the magnetic field, CME shocks generated in the lower corona can have a complex structure including secondary shock fronts, over-compressive and compound shocks, etc. The evolution of these CME shocks is followed during their propagation through the solar wind and, in particular, though the critical points in the wind. Particular attention is given to complex IP events involving two CME shocks colliding to each other, as often observed. The CME shocks are important for 'space weather' because they can easily be observed in radio wavelengths. This makes it possible to track the position of the CMEs/magnetic clouds and, hence, to follow their propagation through the corona.

Key words: CMEs, MHD shock waves, solar wind, CME interaction, numerical simulations.

1. MOTIVATION AND KEY ROLE OF CME SHOCKS

Coronal Mass Ejections (CMEs) play a *crucial role* in space weather and a careful study of the origin, the structure, and the propagation characteristics of these violent phenomena is essential for a deeper insight in space weather physics. The fast CMEs owe their important role to the shock waves they generate. As a matter of fact, the structure of these MHD shocks depends critically on the velocity, the magnetic field, etc. Steinolfson and Hundhausen (1990) predicted that, when these shocks are in the switch-on regime (see below), the shock front must be dimpled in order to avoid a discontinuity at the top. Later, De Sterck and Poedts (1999a) showed that, in this case, such a dimpled shock front is indeed found in numerical simulations (see Fig. 1). Moreover, the shock topology turned out to be rather complex involving almost all different MHD shock types simultaneously, including fast, fast switch-on, intermediate, *double compound*, slow, hydrodynamic, tangential discontinuities, etc. As the topology of these MHD shocks depends critically on the parameter values, e.g. the velocity of the CME and the plasma beta, this may help to derive some of the values of these parameters provided these shocks can be observed in detail in the low corona. In the mean time, Terasawa et al. (2002) carefully investigated the Bastille day event. Their multi-satellite triangulation of data from 5 different spacecraft yielded the 3D geometry of the IP shock generated by this event. It turned out that the shock front is indeed dimpled, which is a clear magnetic (MHD) effect.

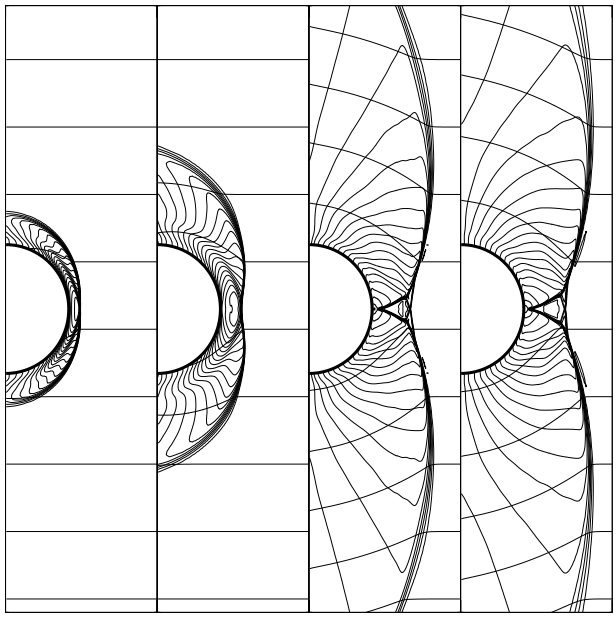

Figure 1. Four snapshots of a symmetric 2D MHD simulation of a plasmoid ejected at high speed in the corona from De Sterck and Poedts (1999a). The right plot is the steady state. The density contour lines pile up in shocks. The magnetic field lines are also shown.

There is another reason why CME shocks are important for space physics: the shocks generated by CMEs can be observed in the interplanetary (IP) medium since they accelerate particles and these particles emit radio waves (see e.g. van der Holst et al. (2002) and references therein). The frequency drift of the resulting type-II radio emissions are related to the dynamics of the shock (and the related CME) from the high corona into the interpla-

netary medium. Changes in the shock and CME dynamics can be caused by interaction with structures in the interplanetary space, e.g. collision with another CME, which can lead to shock–dense matter (dense core of an ejected filament) or shock–shock interaction (Gopalswamy et al. (2001)).

Clearly, the theoretical modeling of the evolution of CMEs can be divided into sub-problems. The first sub-problem is the observational study and modeling of the fast and slow 'quiet' solar wind. The questions regarding, e.g., the heating source(s) and acceleration mechanism(s), the required amount of energy, and the location of the acceleration and heating sources of the fast wind component need to be answered. A second sub-problem is the initiation of CMEs. Why do CMEs occur at all and how are they triggered? Next, there is the sub-problem of the propagation of CMEs and, in particular, the time-height curves need to be understood. Also the evolution of the structure of the CMEs and the leading shock fronts during their propagation through the interplanetary medium needs to be studied. The modification(s) of the MHD shock structure may contain important clues for understanding the propagation properties of CMEs. The impact of CMEs or magnetic clouds on the Earth's magnetosphere is another important sub-problem in which the MHD shock complexity is important. The interaction of the CME leading shock front with the bow shock a the Earth's magnetosphere drastically affects the reconnection characteristics of the magnetic field lines and, hence, certainly influences the 'geo-effectiveness' of the magnetic storms. In the present paper, we concentrate on simulations of the evolution of CMEs in the IP medium.

As the CME related *complex MHD shocks may play a* **key role** in the above-mentioned sub-problems we will first briefly discuss the possible components of the complex MHD shocks generated by fast CMEs.

MHD shocks

As is well-known from fluid dynamics, a supersonic flow finds its way around an object by creating a bow shock in front of it. In a magnetized plasma, the magnetic field introduces a preferred direction and, hence, *anisotropy*. Moreover, in the MHD description of such a plasma, there exist *three basic MHD waves*, viz. the Alfvén wave and the slow and fast magnetosonic waves, instead of just sound waves. The anisotropy of these three wave modes results in MHD shocks which can be much more complex than the shocks in hydrodynamic systems which have only one (isotropic) wave speed. The characteristic velocities of the three MHD waves depend on the direction of propagation and for a direction labeled by x, these velocities are denoted by c_{Ax}, c_{sx}, and c_{fx}, respectively. They always (i.e. for any direction x) satisfy the relation $c_{fx} \geq c_{Ax} \geq c_{sx}$.

When the $x-$direction now denotes the direction perpendicular to the shock front, this means there are four possible positions for the normal plasma speed, v_x, viz.

$$[1] \geq c_{fx} \geq [2] \geq c_{Ax} \geq [3] \geq c_{sx} \geq [4],$$

corresponding to four plasma sates satisfying given values for the fluxes of mass, momentum, magnetic field and energy. Each pair of those states satisfies the Rankine-Hugoniot conditions and can thus be connected by a shock. As a result, there exist three types of MHD shocks called 1) **fast shocks**, in which the flow speed drops from super-fast to sub-fast but super-Alfvénic, i.e. from position [1] to [2], in the shock; 2) **slow shocks**, in which the flow speed drops from sub-Alfvénic but super-slow to sub-slow, i.e. from position [3] to [4], in the shock; and 3) **intermediate shocks**, in which the flow speed drops from super-Alfvénic to sub-Alfvénic, i.e. from [1] to [3], from [1] to [4], from [2] to [3], or from [2] to [4]. Some of the properties of these shocks are summarized in Figure 1 (a–c).

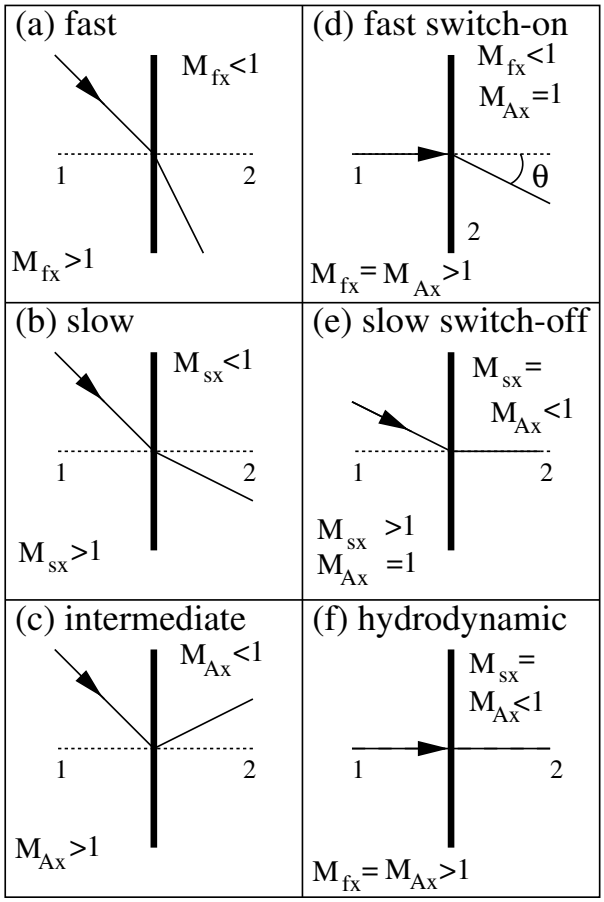

Figure 2. Some properties of basic MHD shocks. The thick vertical line denotes the shock front, the dotted line is the shock normal. The arrowed lines denote magnetic field lines that are refracted through the shock surface. Region 1 is upstream, region 2 downstream. M_{fx}, M_{Ax}, and M_{sx} denote the fast, Alfvén, and slow normal Mach numbers, respectively. (From De Sterck (1999)).

In fast shocks ([1]–[2]) the tangential component of the magnetic field is increased so that the magnetic field lines are refracted away from the shock normal. In slow shocks ([3]–[4]), on the other hand, the magnetic field lines are refracted towards the shock normal, while intermediate shocks change the sign of the tangential component of the magnetic field.

Each of the MHD shock types has a 'limiting case', also indicated in Fig. 2. A fast 'switch-on' shock, e.g., has a vanishing tangential component of the magnetic field upstream, but a finite one downstream, while in a slow 'switch-off' this magnetic field component is 'switched off' by the shock, i.e. it vanishes downstream. A [1]–[4] hydrodynamic shock is a limiting case of an intermediate shock that does not change the magnetic field (see Fig. 2(f)).

Intermediate shocks and fast switch-on shocks can only occur for some well-specified regime of the upstream parameters. Switch-on shocks are intrinsically magnetic phenomena that have no analogue in hydrodynamic flows of neutral fluids. They can only occur when the upstream magnetic field, B_1 is dominant, i.e.

$$B_1^2 > \gamma p_1, \tag{1}$$

and

$$B_1^2 > \rho_1 v_{x,1}^2 \, \frac{\gamma - 1}{\gamma(1-\beta_1)+1}, \tag{2}$$

where $v_{x,1}$ is the upstream velocity component along the shock normal and p_1 and β_1 the upstream thermal pressure and plasma beta, respectively; while γ denotes the ratio of specific heats. These conditions are derived from the Rankine-Hugoniot jump conditions in 1D MHD flows (Kennel et al. (1989); Steinolfson and Hundhausen (1990)).

2. MODELING THE (PRE-EVENT) SOLAR WIND

Wang et al. (1995) showed with a parameter study that the pre-event corona is a crucial factor in dictating CME properties. Hence, we will first discuss the modeling of the solar wind separately. We focus only on those wind solutions used for CME evolution studies.

2.1. Spherically symmetric (1D) wind models

Historical starting points for solar wind models are the Parker (1958) wind, a spherically symmetric (1D), unmagnetized (hydrodynamic) solution; and the Weber & Davis (1967) wind model which constitutes a valuable extension to the rotating, polytropic Parker wind with a radial and toroidal magnetic field component. Later, these one-dimensional models were perfected as ever more physical effects were taken into account. As a matter of fact, such geometrically simple models are still frequently used to study e.g. magnetic loops in closed-field regions of the solar corona or the outflow in coronal holes. They have the advantage that complicated (thermo-)dynamic effects, such as thermal conductivity) can easily included. These 1D models also include at least part of the transition region and radiative losses. Moreover, they are usually not very CPU-intensive. For CME evolution, however, their geometric limitations are a major disadvantage: open and closed magnetic field regions cannot be treated simultaneously in these models.

2.2. Axisymmetric (2D and 2.5d) wind models

Pneuman & Kopp (1971) constructed the first two-dimensional (axisymmetric) MHD model for the solar corona by solving the steady state equations. This model included both a helmet streamer and open field regions. Sakurai (1985, 1990) derived an analytical 2D generalization of the Weber-Davis wind model. Most axisymmetric wind models, however, are numerical solutions obtained by integrating the time-dependent MHD equations by using a time-asymptotic approach. The energy equation is often simplified, e.g. by considering a polytropic relation between pressure and density, sometimes even isothermal. Such simplified polytropic models yield surprisingly good approximations and can reproduce many qualitative features of the observed solar corona. But the plasma density and temperature in these models are not in quantitative agreement with the observations. Therefore, more recent models focus on improving the energy equation. Below, we briefly discuss some of these models that have been used to simulate the evolution of ICMEs and, in particular, the MHD shocks they generate.

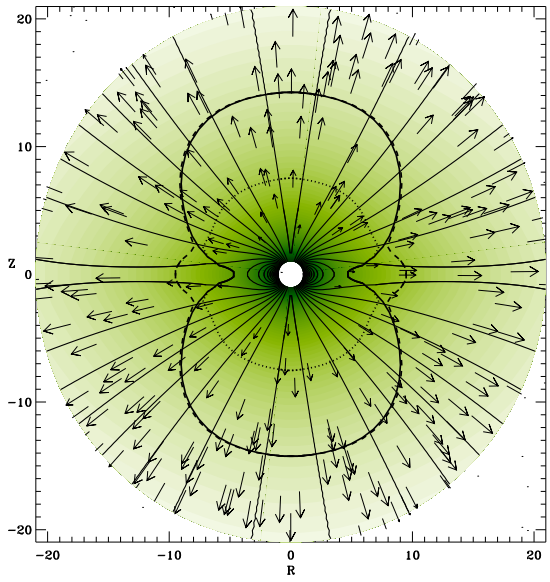

Figure 3. Steady wind solution of Keppens & Goedbloed (1999). The color represents the density (log-scale), black lines are the magnetic field lines, and arrows denote the radial velocity. Also shown are the direction dependent Alfvénic and slow and fast magnetosonic points.

Keppens & Goedbloed (1999, 2000) derived a 2.5D, ideal MHD solution starting from $1.25\ R_\odot$. This polytropic model (with $\gamma = 1.13$) includes differential rotation and both a 'wind' and a 'dead' zone to produce a high speed wind from coronal holes and a low speed wind above streamers. The dead zone is obtained by imposing an initial dipole field and keeping $v_r = 0$ between latitudes $\pm 30^o$. These authors also impose a mass flux $f_{\rm mass} = 0.01377$ in the 'wind' zone, while in the 'dead' zone $f_{\rm mass} = 0$. This wind model, illustrated in Fig. 4 is used to study the effect of the 'dead' zone and the magnetic field strength on stellar wind properties and also to

study CME evolution (see below).

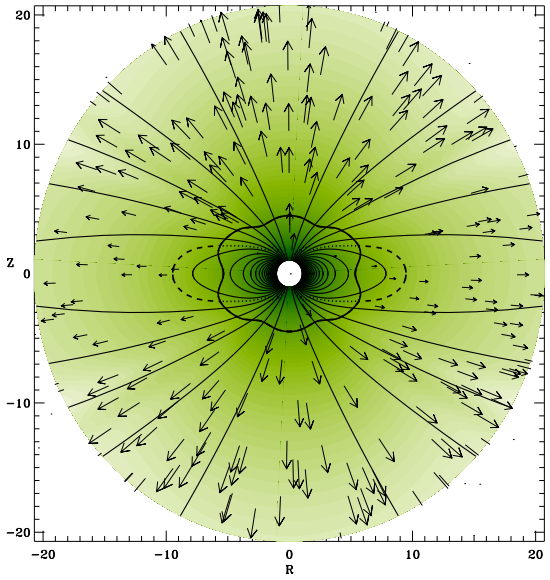

Figure 4. Steady wind solution of van der Holst et al. (2003). The color represents the density (log-scale), black lines are the magnetic field lines, and arrows denote the radial velocity. Also shown are the direction dependent Alfvénic and slow and fast magnetosonic points.

van der Holst et al. (2003) produced a 2.5D, ideal MHD wind solution starting at 1 $R_\odot$ and including differential rotation. These authors initially impose a dipole field (everywhere) and obtain the 'dead' zone effect through a heating source term which takes the form

$$Q = \rho q_0 e^{-\frac{(r-r_0)^2}{\sigma^2}} \left(T_0 - \gamma \frac{p}{\rho} \right).$$

This heating source term is very similar to the volumetric heating function used by Groth et al. (2000).

Wang et al. (1995, 1998) constructed a 2D, polytropic wind solution including both heating and momentum source terms to obtain mass fluxes similar to the empirical solar wind. By combining both constant and latitude-dependent boundary conditions with different values of the polytropic index, these authors showed that the background wind has a drastic effect on the evolution properties of CMEs superposed on it. Later, Suess et al. (1999) upgraded this wind model to a two-fluid MHD model of the global structure of the solar corona which contains collisional energy exchange between electrons and protons. It still includes a momentum source term and the volumetric heat source is different for protons and electrons so that a high T_p/T_e ratio is obtained above the coronal hole and a low T_p/T_e ratio above the streamer.

2.3. Steady, full 3D wind models

Groth et al. (2000) produced a 3D, ideal MHD wind solution with sophisticated Adaptive Mesh Refinement (AMR) finite volume techniques. The solar rotation is imposed through two source terms (centrifugal + coriolis) and the initially imposed magnetic field is multipolar, including terms up to the octupole. Density, temperature and magnetic field are fixed at the base but all velocity components are free there. The heating term has the same form as in van der Holst et al. (2003) (see above) and the Powell source term is applied to keep the magnetic field divergence free.

Mikic et al. (1999) produced another 3D MHD wind solution including a lot of physical effects: thermal conduction, radiative losses, a uniform resistivity and parallel thermal conduction. Moreover, this solution starts at the top of the chromosphere (20000 K) and includes different heating source terms modelling e.g. heating through ohmic and viscous dissipation and through Alfvén wave dissipation. This solution is obtained by imposing an initial potential field, obtained from the extrapolation of the photospheric field, on top of a HD wind solution and relaxing this to obtain the MHD solution which thus takes into account the observed photospheric field. The latter feature guarantees a realistic background wind model which is a great advantage over other 3D wind models, especially when space weather event simulations are envisaged.

3. APPLIED CME INITIATION MODELS

Recently, Klimchuk (2000) reviewed the theoretical models for CME initiation. Based on basic physical properties, such as energetics, structure and dynamics, this author distinguished two types of models, viz. *directly driven* models and *storage and release* models, and presented them making simple analogues involving springs, ropes, and weights. However, *all these models have difficulty explaining one or more aspects of observations.* According to Z. Mikic (on the Shine 2001 meeting) present CME models are too idealized: the geometry is not realistic, there is no fine structure, the models are too dissipative, not fully self-consistent, etc. Hence, a lot of work remains to be done and the present models need to be improved: 3D extensions need to be created including fine structure, real (i.s.o. numerical) dissipation, a realistic shearing of foot points, etc. The numerical methods need to be improved too, e.g. to decrease the numerical dissipation and to capture the shocks formed by fast CMEs.

CME shock evolution studies very often apply *simplified* generation models for the CMEs. Groth et al. (2000) used a 'density-driven' models which simply means that a high-density (and high-pressure) plasma blob is superposed on the solar wind. Other simplified models generate a pressure pulse with or without an additional velocity change (i.e. a kind of 'nozzle' boundary condition), see e.g. Wang et al. (1995); Odstrcil & Pizzo (1999). Keppens & Goedbloed (1999) on the other hand impose an extra mass flow to generate the CMEs (see below).

More realistic CME evolution simulations make use of theoretical analytic CME initiation models such as the models of the self-similar Gibson & Low (1998) family

(Gombosi et al. (2000)) or the Titov & Démoulin model (Roussev et al. (2003)). Odstrcil & Pizzo (2002) and Odstrcil et al. (2002) still use another analytical flux rope model. What one really should do, however, is to simulate the evolution of reconstructed coronal structures (e.g. Aulanier et al. (2000)) driven unstable by foot point shearing and/or flux emergence or cancellation. Several groups are working on such simulations and results will appear in the near future.

4. CME PROPAGATION AND CME-CME INTERACTIONS

The shocks generated by CMEs *can* be observed in the interplanetary (IP) medium due to the fact that they accelerate particles and these accelerated particles emit radio waves. We know that the IP signals of CMEs do not possess the typical three-part structure of most CMEs in the low corona (bright loop, dark void, bright inner kernel). However, a lot of key questions remain to be answered, e.g. How do CMEs propagate through the solar wind? At what speeds?; Can the speed of a CME be constant?; What is the geometrical structure of the associated shocks?; How does the type and geometry of the shocks change at the critical points in the wind?

Evolution of single CMEs

van der Holst et al. (2003) superposed a CME on their 2.5D MHD wind solution discussed above (Fig. 4). They used the simplified 'density(+pressure)-driven' model and simulated CMEs both in the equatorial streamer belt and at larger latitudes (see Fig. 5).

Groth et al. (2000) also simulated 'density-driven' CMEs superposed on their 3D ideal MHD wind solution. Their AMR thechniques allow to study the interactions of the CMEs with the streamer belt in detail. Gombosi et al. (2000) used the same wind solution but a better CME initiation model. These authors superposed an analytical, 3D, 'Gibson & Low ('98) family' self-similar CME in the streamer belt and followed its evolution through the solar wind (see Fig. 6). It is found that the flux rope expands rapidly and drives a strong shock ahead of it. As the CME evolves in IP space, the flux rope is deformed and the MHD shock front propagates at the same speed as the flux rope in the center but far ahead to the sides of the rope. Roussev et al. (2003) considered the Titov & Démoulin flux rope model as initial condition although the evolution of this CME is only simulated in the lower corona. Manchester et al. (2003) focussed on a space weather event simulation in the most numerical technically advanced simulation so far. This most ambitious calculations simulates the CME from its formation at the Sun through its evolution in IP space to its interaction with the magnetosphere-ionosphere system. The CME was generated by a density pulse near the Sun. The simulation used an adaptive mesh refinement (AMR) technique, started with 4.5×10^6 computational cells and ended with 14×10^6 cells (see Fig. 7).

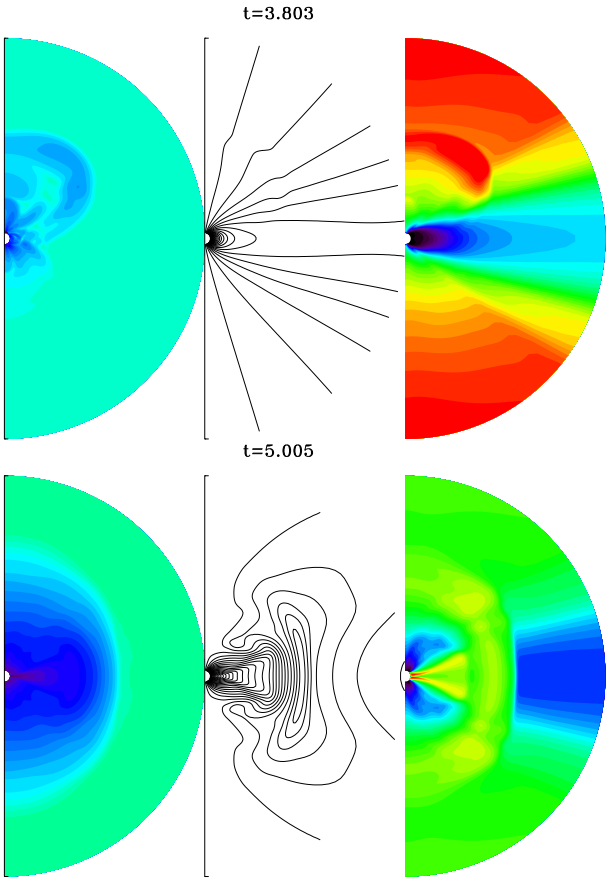

Figure 5. CME superposed on solar wind, above: near the pole, below: in the streamer belt. Left panel: density, center: magnetic field, right panel: radial velocity minus the wind velocity.

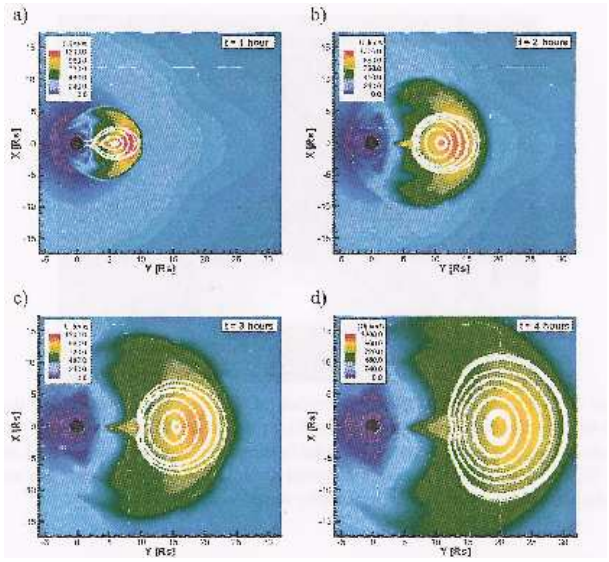

Figure 6. Evolution of the Gibson & Low (self-similar) CME model in IP space. Solid white lines display magnetic streamlines superimposed on a color image of the velocity magnitude.

Odstrcil & Pizzo (1999) also first used simplified CME models (an over-pressured spherical plasmoid) and follo-

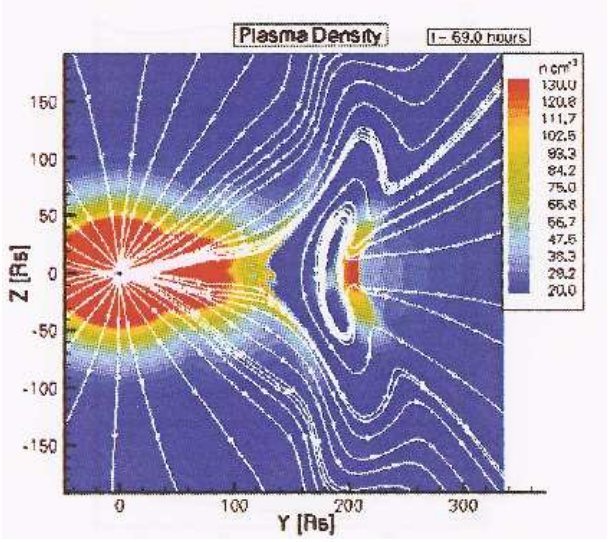

Figure 7. Most ambitious space weather simulation so far. Meridional cut through a CME as it approaches the Earth about 67 hours after initiation. Color code: plasma density, white lines: projected magnetic field lines.

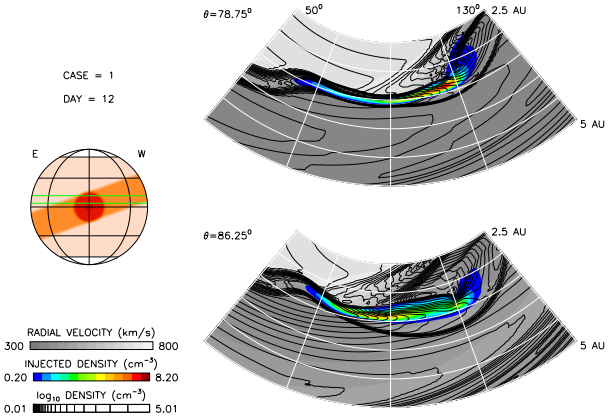

Figure 8. Longitudinal cross-sections of a CME 12 days after launch from the inner boundary near the Sun. Grey scale: velocity distribution, color scale: injected number density, contours: total number density, shown in two slices at co-latitudes 78.75^o (top) and 86.25^o (bottom), slice positions are also inidcated on the left (green lines).

wed the CME for a long time (up to 5 AU). They showed that the CME interacts strongly with the co-rotating streamer belt and that this interaction can be very complex. The initially spherical CME is completely deformed due to this interaction which generates both a forward and a reverse shock front (shock-pair structure) in the co-rotating interaction region (CIR). The CME is trapped between the slow streamer belt flow and the fast coronal hole flow and is squeezed within the CIR structure. The CME-driven shock has varying stand-off distances ahead of the CME and gradually merges with the forward CIR shock (see Fig. 8). Later, Odstrcil & Pizzo (2002) used a more realistic analytical flux-rope model for the CME and studied the compression of the flux rope and the evolution of the dimpled leading shock front (see Fig. 9 and also Odstrcil (2003)). Odstrcil et al. (2002) also demonstrated the merging of coronal and heliospheric 2D MHD models developed at SAIC San Diego and CU/CIRES-NOAA/SEC Boulder. These models are quite different as regards the included physics and the used numerical techniques and grids over their respective spatial and temporal domains. Odstrcil (2003) also presented results of ongoing coupled 3D MHD simulations of a fast-moving magnetic flux rope that stretches from the Sun through the model interface boundary into the heliosphere. The corresponding IP shock compresses the plasma density ahead of the magnetic flux rope and the shock front is distorted (dimpled) due to the interaction with the slower solar wind around the heliospheric current sheet.

CME-CME interactions

According to Burlaga (Shine 2001 meeting, USA) two thirds of the interplanetary ejecta are complex, i.e. last several days and may consist of two or more CMEs coming together. The 'Bastille-day' event, e.g., produced 5 CMEs with their corresponding shocks overtaking each other. Hence, the interactions of different ejecta need to be studied in order to understand the observations. Gopalswamy et al. (2001) made a detailed and careful analysis of radio observations of two CMEs at different speeds originating from the same region on the Sun. The leading shocks of both CMEs collide and emit a complex radio spectrum. Such well-documented events are perfect candidates for case studies.

In hydrodynamics, it is well-known that when two shocks collide the two discontinuities merge into one discontinuity that no longer satisfies the Rankine-Hugoniot condition(s). Several scenario's are possible. The observation of Gopalswamy et al. (2001) seems to correspond to the case where two shocks of the same family collide, resulting in a shock in that same family. However, such a shock collision also causes a rarefaction wave and there is no sign of this rarefaction in the dynamic radio spectrum, probably because it is too weak to accelerate particles.

At the CPA we initiated the study of IP CME interactions with investigations of 1D HD and MHD shock interactions superposed on a background 1D wind model. More recently a parameter study was performed of CME shock interaction in 2.5D MHD. Starting point was the 2.5D polytropic wind of Keppens & Goedbloed (1999). The CMEs considered are associated with sudden, significant mass losses causing violent disruptions of the global magnetic field pattern. They are triggered on top of the outflow pattern. The calculations are restricted to 2.5D (axisymmetric). In future work, we intend to model the CMEs in a more realistic way. Here, the CMEs are generated in the same way as Keppens & Goedbloed (1999) did, i.e. by means of a modification of the boundary condition imposed on the poloidal momentum equation, namely

$$\rho \mathbf{v}_p = \frac{f_{\rm mass}}{r^2} \hat{\mathbf{e}}_r,$$

with an extra mass flux in the form:

$$f_{\rm mass}(\theta, t) \quad = \quad f_{\rm wind}(\theta) + \qquad (3)$$

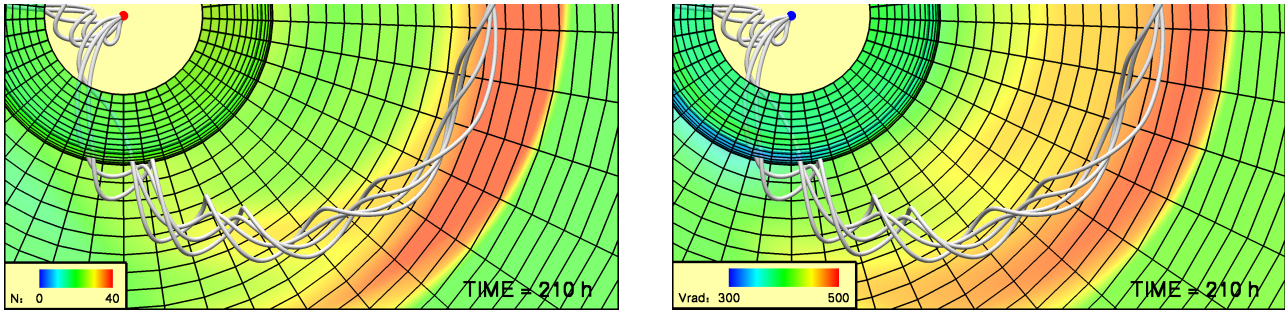

Figure 9. Selected magnetic field lines (in 3D) of a flux rope expanding into IP space. Left: number density; right: radial velocity in the equatorial plane and on the interface between coronal and heliospheric models.

$$g_{\rm cme} \sin \frac{\pi t}{\tau_{\rm cme}} \cos^2 \left(\frac{\pi}{2} \frac{\theta - \theta_{\rm cme}}{\alpha_{\rm cme}} \right),$$

for $t_0 \leq t \leq t_0 + \tau_{\rm cme}$ and $\theta_{\rm cme} - \alpha_{\rm cme} \leq \theta \leq \theta_{\rm cme} + \alpha_{\rm cme}$. The wind-related mass-loss rate $f_{\rm wind}(\theta)$ contains the polar angle dependence due to the dead zone, as explained in the previous section. The extra four parameters control the CMEs. The parameter $g_{\rm cme}$ controls the CME mass-loss rate, $\tau_{\rm cme}$ its launch time interval (i.e. its duration), $\theta_{\rm cme}$ its location or launch angle, and $\alpha_{\rm cme}$ its angular width (i.e. its extent in polar angle). The first CME is launched starting at $t = 0$ while at a later time interval, ranging from t_0 to $t_0 + \tau_{\rm cme2}$ a second CME is launched. Below time is given in units of 87 minutes. For the parameters:

	$g_{\rm cme}$	t_0	$\tau_{\rm cme}$	$\theta_{\rm cme}$	$\alpha_{\rm cme}$
$\rm CME_1$	0.5	0	1	18°	18°
$\rm CME_2$	1.5	5	2	18°	18°

the temporal evolution of the two CMEs is illustrated in Fig. 10.

Note that the total amount of mass lost due to the CMEs depends on all four parameters. The total mass loss $M_{\rm cme}$ can be evaluated from:

$$M_{\rm cme} = 2\, g_{\rm cme}\, \tau_{\rm cme} \frac{\pi^2}{\pi^2 - \alpha_{\rm cme}^2} \times [\cos(\theta_{\rm cme} - \alpha_{\rm cme}) - \cos(\theta_{\rm cme} + \alpha_{\rm cme})]. \quad (4)$$

For the first CME, the above parameter values yield a total mass loss of 1.06×10^{13} kg. For the second CME the total mass loss is six times higher.

In the parameter study, the properties of the first CME were fixed while the properties of the second CME were varied. Even when the 2nd CME is slower than the first one, its evolution is influenced by the first CME due to the effect on the IP space of the latter. First, the parameter $g_{\rm cme2}$ was varied. It was found that the more massive the second CME, the stronger the interaction of the two CMEs, i.e. the larger the acceleration of the first CME and the higher the final velocity. Clearly, the interaction is more interesting and complex when both CMEs are comparable. When the second event is much more powerful and massive than the first event, the result is a 'walk-over' by the second CME. In Fig. 11 we illustrate the interaction of two CMEs launched in the same direction (18^o) by ten snapshots of the radial velocity profile on a cross-section in the middle of the leading shock front. From this figure it is clear that the two shock fronts collide and continue to propagate as a single shock. One may get the impression, however, that the second CME is slightly accelerated by the interaction. Therefore, in the second part of the figure, we subtracted the velocity of the background wind. From this figure it is clear that both CMEs decelerate but the second CME decelerates slower than the first one. The net result of the interaction is a slower deceleration of the second CME.

We also varied the parameter $\tau_{\rm cme2}$, i.e. the time span of the second CME. This parameter was varied between 87 minutes and up to 261 minutes. The effect of this parameter is very similar to the effect of the previous one: the longer the second CME lasts, the stronger the interaction is and the larger the width of the final IP disturbance.

Next, we varied the launch angle $\theta_{\rm cme2}$ of the second CME while the launch angle of the first CME was fixed to 18^o. We considered the values 18^o, 36^o, and 72^o. Notice that the total mass of the second CME is influenced by this parameter. When the launch angle of the two CMEs is different, the second CME needs more time to catch up with the first one. Clearly, the final CME has a larger width in this case. Also, the interaction is most pronounced in between the two launch angles and stronger the smaller the difference in launch angle of the two CMEs is. This is illustrated in Fig. 12 where again snapshots of the radial velocity profile (after subtraction of the background wind velocity) are plotted along two different cross-section of the final shock front. The first cross-section is made at 18^o, i.e. through the center of the shock of the first CME. The second cross-section is made at 27^o, i.e. through the middle of the two launch angles, since in this case $\theta_{\rm cme2} = 36^o$. It is clear that the interaction is θ-dependent and complex. It seems to result in an acceleration at $\theta = 27^o$. Due to the θ-dependence of the interaction, the final shock front is deformed.

Finally, also the parameter $\alpha_{\rm cme2}$ was varied. The values 18^o, 36^o and 54^o were considered. Notice that the total mass of the second CME is influenced by this parameter too. A larger width of the second CME results in a faster interaction with the first CME, whose parameters are not changed in this study. The larger the width of the second CME, the stronger the interaction. A typical result is shown in Fig. 13.

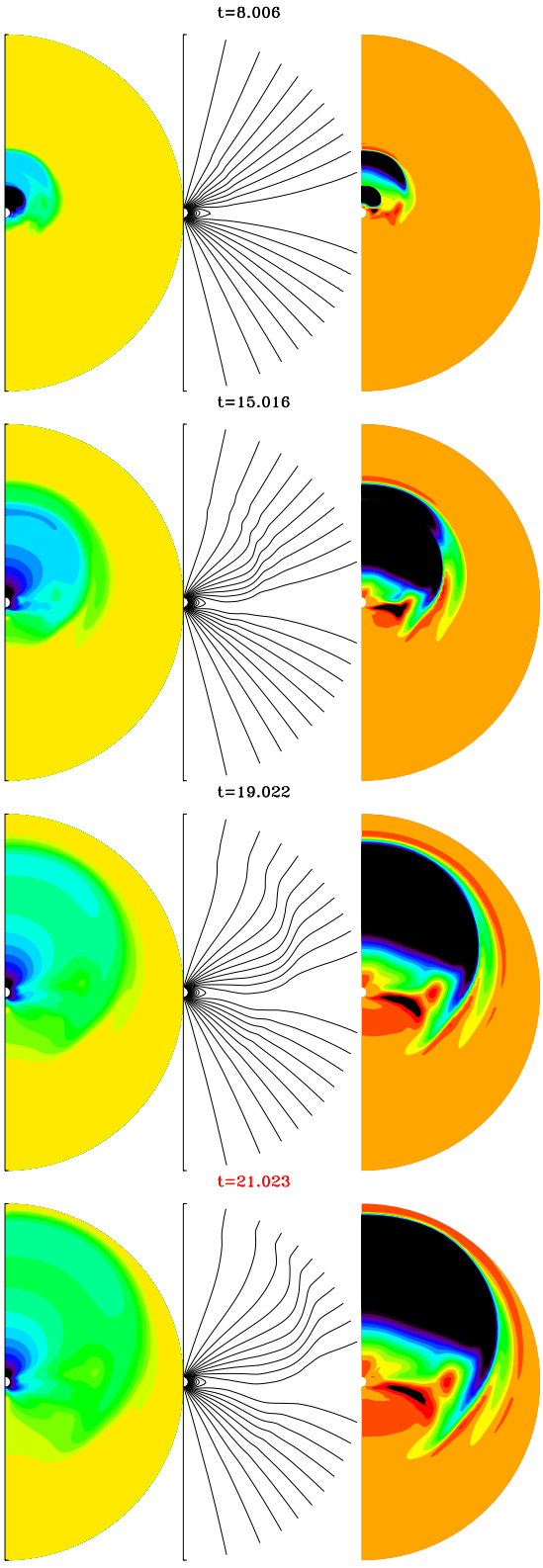

Figure 10. Four snapshots of the evolution of 2 subsequent CMEs. Left panel: the density difference between the evolving mass ejection and the background solar wind. Middle: the magnetic field structure. Right panel: $v_r - v_{\rm wind}$. Time is normalized: $1 = 87$ min. The simulation domain reaches from 1 up to roughly 36 solar radii.

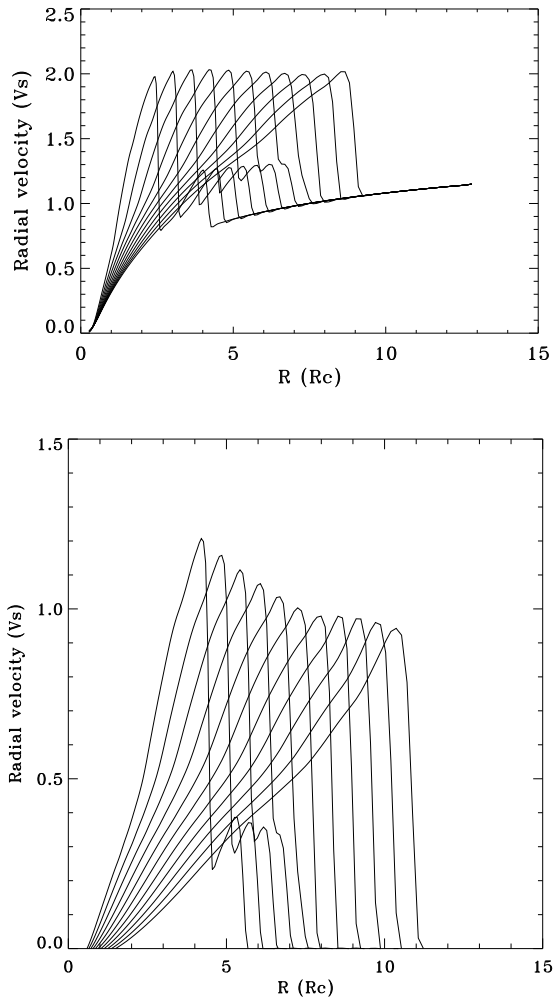

Figure 11. Above: snapshots of the cross-section of the radial velocity profile at $theta = 18^o$, i.e. through the center of the shock front. Below: idem but here the background solar wind speed is subtracted form the radial velocity.

Remark that the above parameter study is just a simple first attempt to investigate the interaction of IP CMEs. For definitive conclusions one needs more realistic simulations and more extensive parameter studies which also include, e.g., the magnetic field parameters. Such studies are not frequent in the literature. Odstrcil et al. (2002) studied the collision and interaction of two magnetic flux ropes and showed that the two flux ropes merge and continue to propagate as a single flux rope. Clearly, these parameter studies need to be extended and improved.

5. CONCLUSIONS

The *pre-event solar atmosphere* has a substantial influence on the CME evolution. For this solar wind there exist many advanced 1D, 2D, and 3D steady models with state-of-the-art numerical techniques and/or a lot of physical effects included. Yet, these models are all steady models which are still far away from a realistic,

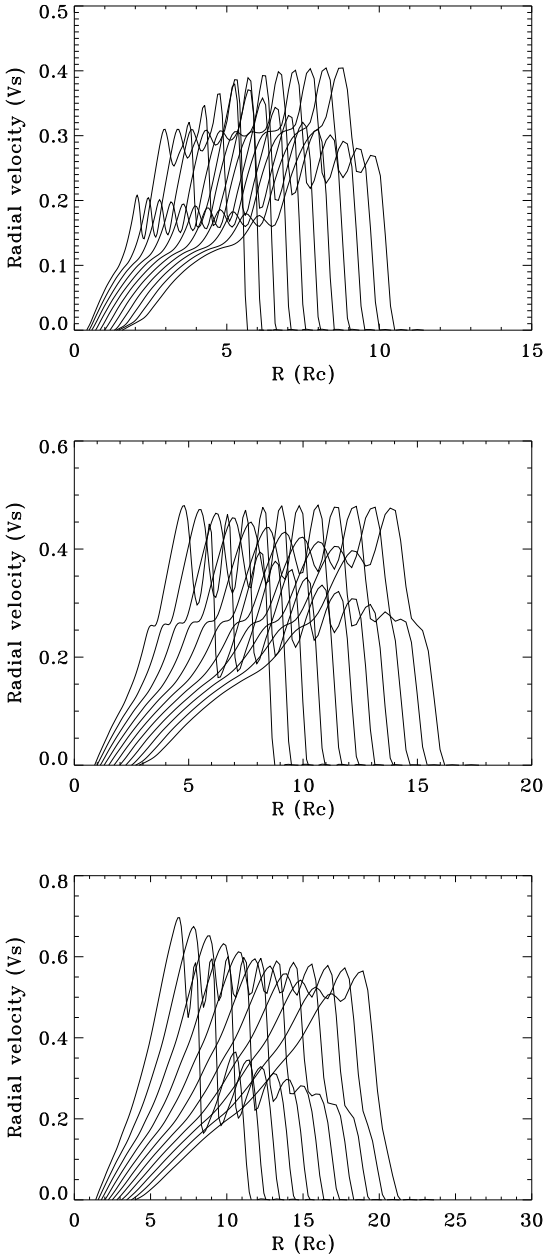

Figure 12. Above: snapshots of the cross-section of $v_r - v_{\rm wind}$ at $\theta = 18^o$, i.e. through the center of the first CME shock front. Middle: idem at $\theta = 27^o$, i.e. through the center of the two launch angles $\theta_{\rm cme1}$ and $\theta_{\rm cme2}$. Below: idem at $\theta = 36^o$, i.e. through the center of the shock front of the second CME.

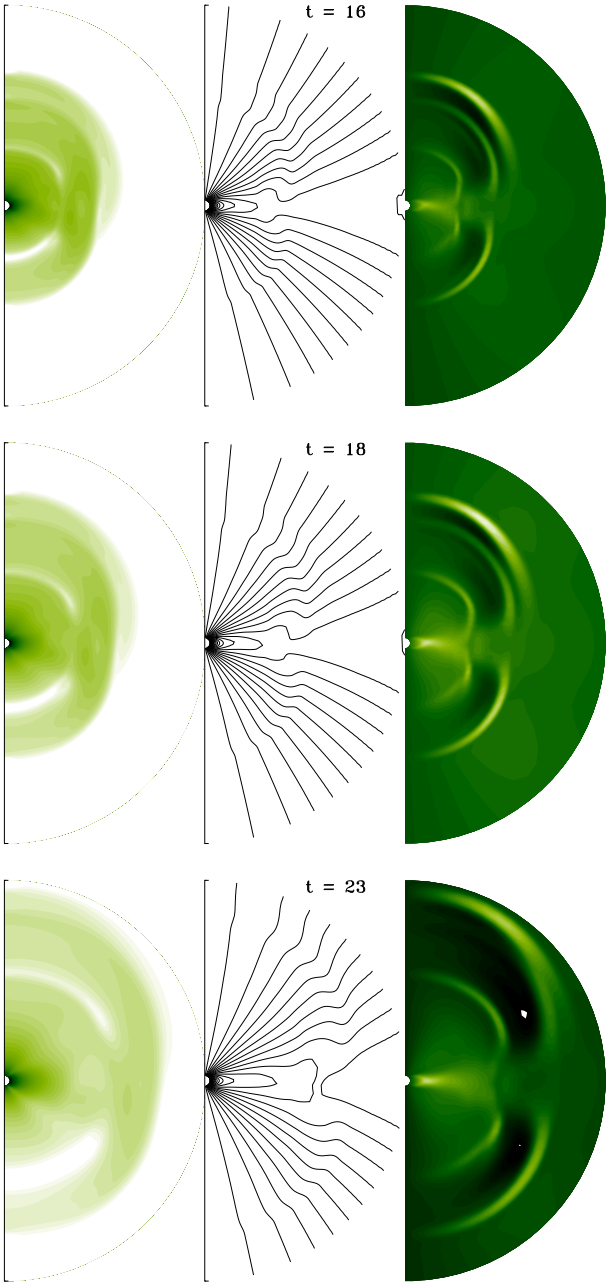

Figure 13. Three snapshots evolution of 2 subsequent CMEs. Left panel: the density difference between the evolving mass ejection and the background solar wind (log-scale). Middle: the magnetic field structure. Right panel: the v_φ velocity component. Time is normalized: $1 = 87$ min. The simulation domain reaches from 1 up to roughly 36 solar radii.

high-resolution, real-time unsteady model. Moreover, the present wind models use a lot of additional (artificial) heating and/or momentum source terms which demonstrates and circumvents our lack of physical insight. Also, there are only a few attempts so far to include non-MHD effects, at least in the solar wind models used for CME evolution studies.

The present 2D and 3D *CME initiation models* still have a lot of problems explaining the observations. The are not frequently used in current CME evolution studies. As a matter of fact, CME evolutions simulations most often use simplified, density- and/or pressure-driven models. Here, empirical models based on magnetograms and reconstructed coronal magnetic fields would be more realistic, especially when superposed on real-time solar wind model.

Very advanced 3D unsteady models exist for *the evolution of CMEs* through the IP space. The most advan-

ced numerical techniques are being combined with the most advanced models regarding physical content. Yet, most simulations so far concentrate on the evolution of a single CME. Most IP magnetic clouds, however, are complex and consist of two or more CMEs coming together. Hence, such CME collisions should be investigated in more detail to get insight in the evolution and effects of propagating IP ejecta.

ACKNOWLEDGMENTS

These results were obtained in the framework of the projects OT/02/57 (K.U.Leuven), 14815/00/NL/SFe(IC) (ESA Prodex 6), and the European Community's Human Potential Programme contract HPRN-CT-2000-00153, PLATON, also acknowledged by B. vdH.

REFERENCES

Aulanier G., DeLuca E.E., Antiochos S.K., et al., 2000, ApJ 540, 1126–1142

De Sterck H., 1999, PhD thesis, NCAR/CT 167.

De Sterck H. and Poedts S., 1999, A&A 343, 641–649

De Sterck H. and Poedts S., 1999, *in Proceedings of the 9th European Meeting on Solar Physics*, Florence, ESA-SP-448, 935–942

De Sterck H. and S. Poedts, 1999, JGR 104, 22401

Gibson S., Low B.C., 1998, ApJ 493, 460–473

Gombosi T.I., DeZeeuw D.L., Groth C.P.T., Powell K.G., Stout Q.F., 2000, J Atm and S-T Phys 62, 1515–1525

Gopalswamy N., Yashiro S., Kaiser M.L., Howard R.A., Bougeret J.-L., 2001, ApJ 548, L91-L94

Groth C.P.T., De Zeeuw D.L., Gombosi T.I., Powell K.G., 2000, JGR 105, 25053–25078

Kennel C.F., Blandford R.D., Coppi B., 1989, JPP 42, 299–319

Keppens R., Goedbloed J.P., 2000, ApJ 530, 1036–1048

Keppens R., Goedbloed J.P., 1999, A&A 343, 251–260

Klimchuk J.A.: Proc. of the Chapman Conference on Space Weather, AGU, Geophysical Monograph Series 125, eds. P. Song, H. Singer, and G. Siscoe, 2001, 143–157.

Linker J.A., Mikic Z., ApJ 438, L45-L48

Manchester W.B., Gombosi T.I., Roussev I.I., De Zeeuw D.L., Sokolov I.V., Powell K.G., Tóth G., Opher M., 2003, AGU Proceedings, in press.

Mikic Z., Linker J.A., Schnack D.D., Lionello R., Tarditi A., 1999, Phys. Plasmas 6, 2217–2224

Odstrcil D., Pizzo V.J., 1999, JGR 104, 483–492 and 493–503

Odstrcil D., Pizzo V.J., 2002, ESA SP-477, 293–296

Odstrcil D., Linker J.A., Lionello R., Mikic Z., Riley P., Pizzo V.J., Luhmann J.G., 2002, JGR 107, 10.1029/2002JA009334

Odstrcil D., Vandas M., Pizzo V.J., MacNeice P., 2002, Proc. Solar Wind 10, in press.

Odstrcil D., these proceedings.

Parker E.N., 1958, ApJ 128, 664–676

Pneuman G.W., Kopp R.A., 1971, SPh 18, 258–270

Riley P., Linker J.A., Mikic Z., 2001, JGR 106, 15889–15901

Roussev I.I., Forbes T.G., Gombosi T.I., Sokolov I.V., DeZeeuw D.L., Birn J., 2003, ApJ 588, L45-L48

Sakurai T., 1985, A&A 152, 121.

Sakurai T., 1990, Comput. Phys. Rep. 12, 247.

Steinolfson R.S., Hundhausen A.J., 1990, JGR 95, 20693–20699

Suess S.T., Wang A.H., Wu S.T., Poletto G., McComas D.J., 1999, JGR 104, 4697–4708

Terasawa T., et al., 2002, Proc. First Stereo Workshop, Paris, in press.

Titov V.S., Démoulin P., 1999, A&A 351, 701–720

van der Holst B., Van Driel-Gesztelyi L., Poedts S., 2002, ESA SP-506, 71–74

van der Holst B., Poedts S., Chattopadhyay I., Banerjee D., 2003, to be submitted

Wang A.H., Wu S.T., Suess S.T., Poletto G., 1995, SPh 161, 365–381

Wang A.H., Wu S.T., Suess S.T., Poletto G., 1998, JGR 103, 1913–1922

Weber E.J., Davis L.Jr, 1967, ApJ 148, 217–227